MDPI

Thrust-Bearing Layout Design of a Large-Sized Hydrostatic Rotary Table to Withstand Eccentric Loads for Horizontal Boring Machine Applications

Hua-Chih Huang * and Shen-Hen Yang

Department of Mechanical Engineering, National Kaohsiung University of Science and Technology, Sanmin District, Kaohsiung City 80778, Taiwan; peteryang123456@gmail.com
* Correspondence: hc.huang@nkust.edu.tw; Tel.: +886-7-381-4526

Abstract: There is an increasing demand for large-sized hydrostatic rotary tables due to the industrial need for the precision machining of large workpieces for wind generation, aerospace, shipbuilding, and national defense applications. As a consequence, under eccentric loads, the deformation of the large-sized hydrostatic rotary table of a horizontal boring machine would negatively affect machining precision. Indeed, the hydrostatic thrust-bearing recess layout design is the main factor that affects the rotary table's resistance against deformations caused by eccentric loads. This study focused on the capillary-compensated constant-pressure large-sized hydrostatic rotary table for a horizontal boring machine. ANSYS software was used to simulate the thermal and structural deformation of the worktable under eccentric loads. In addition to the original layout of the hydrostatic thrust bearing, three other bearing recess layouts, which involved two different recess diameters, were designed in order to examine the deformation of the worktable under eccentric loads. The results showed that, in terms of a single-ring hydrostatic thrust-bearing layout, a larger recess diameter resulted in a smaller worktable deformation compared to a smaller recess diameter; in terms of a dual-ring hydrostatic thrust bearing layout, the worktable deformation was smaller than that of the single-ring layout with a larger recess diameter. Under the spatial and geometric constraints of the worktable, adopting a hydrostatic thrust bearing with a dual-ring recess layout would minimize the worktable deformation under eccentric loads. For thermal deformation in a single-ring hydrostatic bearing pad layout, however, a larger recess diameter resulted in a larger worktable thermal deformation compared to a smaller recess diameter.

Keywords: hydrostatic rotary table; hydrostatic thrust bearing; eccentric loads; bearing recess layout

1. Introduction

A horizontal boring machine allows boring, drilling and milling in a single setup, thus effectively enhancing the machining efficiency of large workpieces. Horizontal boring machines are widely applied in the military, aerospace, shipbuilding, and wind generation industries. The rotary table of a conventional horizontal boring machine has a functional design that includes a linear slideway system with a linear feed drive as well as a rotary table. Since horizontal boring machines are mainly used in the machining of large workpieces, in order to bear the weight of these large workpieces, the machines are generally equipped with a complete hydrostatic bearing design, i.e., a hydrostatic rotary table with a closed-type hydrostatic slideway system.

Hydrostatic bearings provide excellent performance in terms of positioning resolution, damping property, motion smoothness, and load carrying capacity [1]. These characteristics are especially suitable for precision/heavy-duty machine tool applications. A substantial literature has described the design of hydrostatic bearings with capillary restrictors [2–5]. In 2012, Lee et al. [6] optimized the hydrostatic rotary table of a floor-type boring machine as a lightweight and high-rigidity structure by using a FEM structural analysis and a

genetic algorithm. In 2013, Shie and Shih [7] studied the optimization of the uniform pressure distribution of three different chamber-sets in a hydrostatic rotary table by using a hybrid Taguchi genetic algorithm and Gray relational analysis to obtain the optimal parameters of bearing surface recess. Wang et al. [8] investigated the effect of the oil state (sufficient/deficient state) on the temperature field distribution and temperature rise of heavy-duty hydrostatic bearing. Based on the principles of fluid dynamics, lubrication theory, and the finite volume method, Srinivasan [9] employed repetitive algorithms to perform numerical calculations on the conditions of the two-dimensional oil film pressure fields in thrust bearings that supply oil at constant flow rates. The results indicated that with increasing rotary table rotational speed, the pressure of the oil recess remained unchanged, while its temperature gradually increased. In 2014, Zhao et al. [10] analyzed the bearing capacity of the oil pocket with and without the mass offset of the hydrostatic worktable of a gantry moving milling center. Zhang [11] studied the parameters of the slide table of a heavy-duty CNC floor-type boring machine with a constant-pressure oil supply system. The author pointed out that the initial oil film should not be too thick and that the thickness should range between 30 to 60 μm, so as to avoid instability in the hydrostatic slideway of the heavy-duty machine tool. Zhang et al. [12] performed a systematic analysis on the thermal deformation field of a hydrostatic bearing rotary table and its disciplinary guidance for the production of a hydrostatic bearing table in 2015. In 2016, Wang et al. [13] found that the uneven pressure distribution and the temperature rise of lubricant film in the resistive oil edge of a hydrostatic circular pad were related to the increase in dimensionless hydrodynamic parameters due to the thermal and hydrodynamic coupling effect. Wang et al. [14] showed that the deviation of the oil film thickness and the dynamic performance of the hydrostatic rotary table were reduced by unbalance loading. In 2017, Wang et al. [15] designed the geometrical parameters of oil pads on a hydrostatic turntable to minimize energy consumption by using particle swarm optimization. In 2018, Chang [16] proposed design changes to the effective recess area of the axial thrust bearings in a horizontal boring machine worktable, such that the most suitable bearing pressure could be obtained under desired loads. Fundamental and pioneering research works of stepped or tapered thrust bearings have been performed intensively since the early 1950s by Kettleborough et al. [17–25], mainly in the form of solution methods of pressure, temperature and vibration, experimental investigation, and applications. Thermal designs of thrust bearings were critical in applications that were discussed by Gohar and Rahnejat [26] and other researchers [27–30]. In summary, the aforementioned literature focused on either the modeling or the analysis of three fields: (i) the structural deformation of hydrostatic rotary table under loading, (ii) the temperature rise in or thermal deformation of the bearing pad, (iii) optimized bearing pad design for maximum load capacity. However, none of these studies discussed the layout design of hydrostatic thrust bearings to withstand the eccentric load in a hydrostatic rotary table.

This study focuses on a capillary-compensated large-sized hydrostatic rotary table for horizontal boring machine applications. One-way fluid–solid interaction was modeled through ANSYS software (version 19.0) to simulate and analyze the thermal deformation and the eccentric loading condition of the rotary table structure in the original and three different recess layouts of the hydrostatic thrust bearing. Based on the simulation results, the study then compares the advantages and drawbacks of the original and the three different recess layouts on the structural deformation under eccentric loads, as well as the thermal deformation of the hydrostatic rotary table. Finally, the study discusses the best recess layout in the hydrostatic thrust bearing of a large-sized eccentric load-resistant hydrostatic rotary table for horizontal boring machine applications. The research results of this study can provide some design guidelines for the bearing-pad layout design of a large-sized hydrostatic rotary table to withstand eccentric loads.

2. Model and Research Method

2.1. Introduction to the Research Model

2.1.1. Structural Analysis of the Model

Figure 1 depicts the hydrostatic slideway rotary table in this study. It is a uniaxial linear hydrostatic slideway system consisting of one hydrostatic rotary table on top of the linear guide-table [31]. Its external dimensions (2200 mm × 1800 mm) are shown in Figure 2. Figure 3 shows the internal structure of the gear connector and the configuration of the hydrostatic bearing pads inside the rotary table. The main components include a hydrostatic journal bearing, a gear connector, and a hydrostatic thrust bearing. The dimensions of the oil recess of the hydrostatic thrust bearing are detailed in Figure 4 and Table 1. The diameter of the oil recess in its original layout is shown in Figure 5.
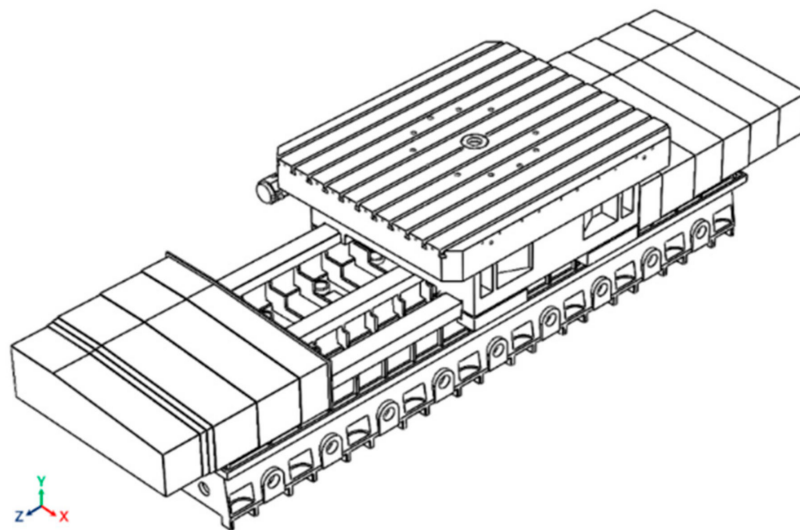

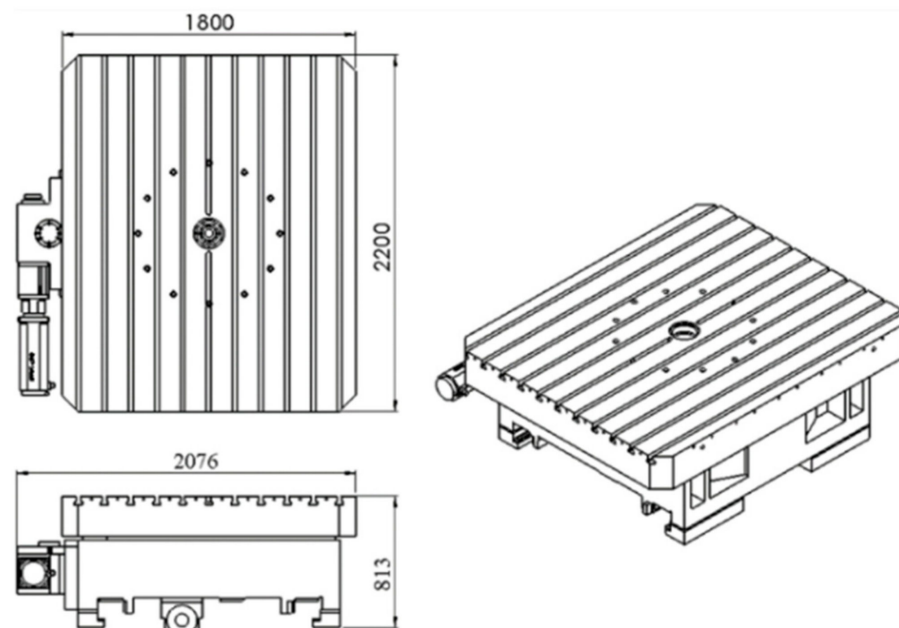**Figure 1.** Hydrostatic slideway rotary table.
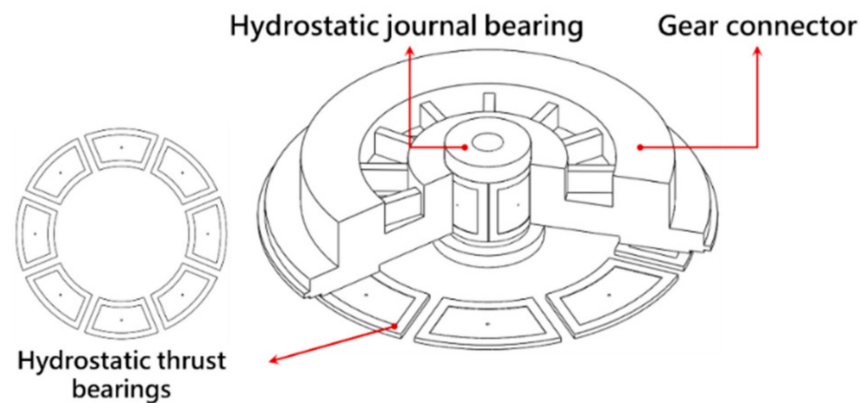

Figure 2. Dimensions of rotary table.

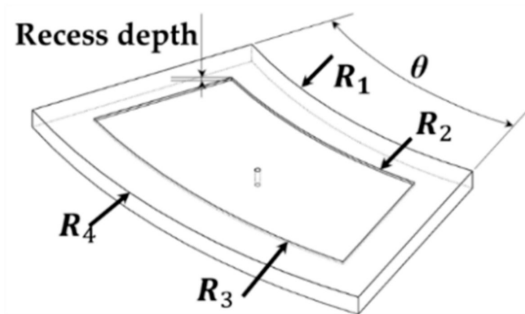**Figure 3.** Structure of the hydrostatic rotary table.

Figure 4. Oil recess of hydrostatic thrust bearing.

Table 1. Dimensions of the hydrostatic thrust bearing's oil recess.

Size Position	Thrust Oil Recess
θ (deg)	35
R1 (mm)	371
R2 (mm)	404
R3 (mm)	544
R4 (mm)	577
Effective area (m^2)	0.045
Recess depth (mm)	2

In order to examine the effects of the structural design of the hydrostatic thrust bearing on the thermal and structural deformation of the rotary table, this study made isogonic modifications to the dimensions of the planar fan-shaped recess according to the recess angle (θ). Two recess designs with different dimensions but with the same effective area were yielded. The external dimensions of the recesses are shown in Figure 6 and detailed in Table 2. Several combinations were made based on these two recesses, which resulted in the three recess layouts depicted in Figure 7, described as follows:

Layout I: A single-ring recess layout that uses the minimum-diameter recess; the diameter (ø) is 1059 mm, and the internal diameter of the recess (R1) is aligned with the internal diameter of the connector.
Layout II: A single-ring recess layout that uses the maximum-diameter recess; the diameter (ø) is 1228 mm, and the external diameter of the recess (R4) is aligned with the external diameter of the connector.
Layout III: A dual-ring recess layout in which the positions of the minimum-diameter recess and the maximum-diameter recess are staggered.
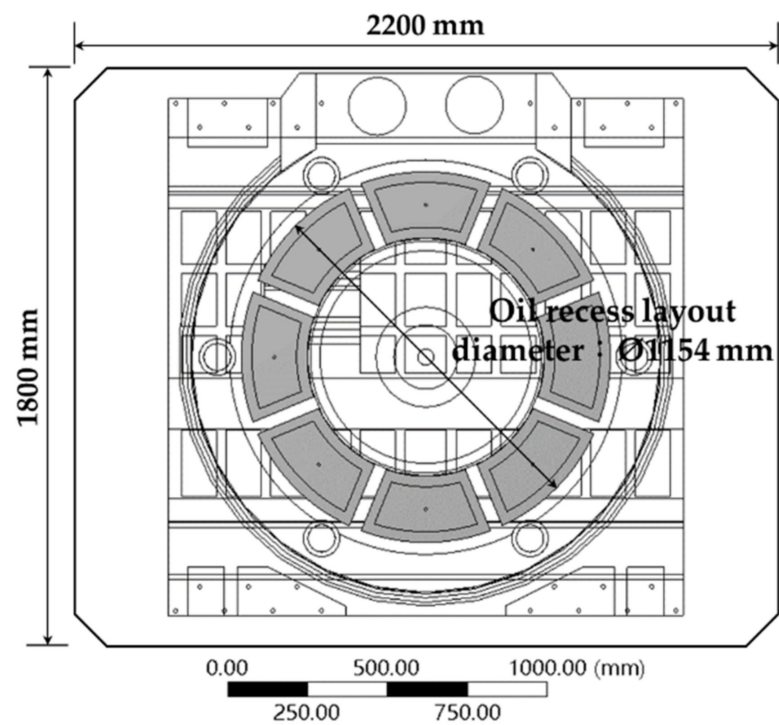
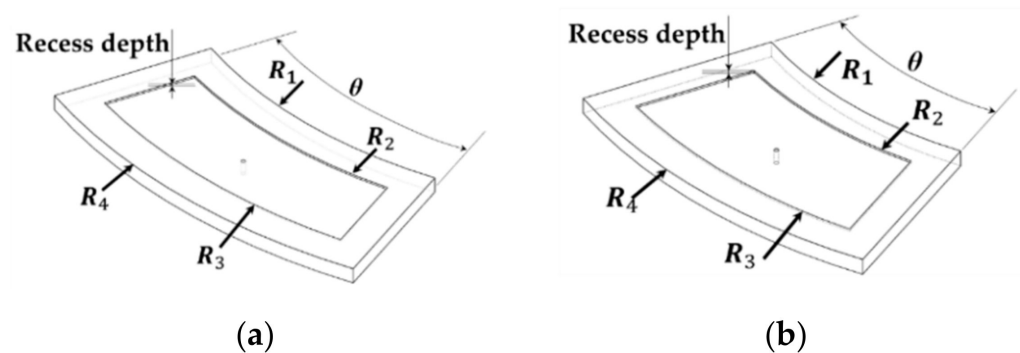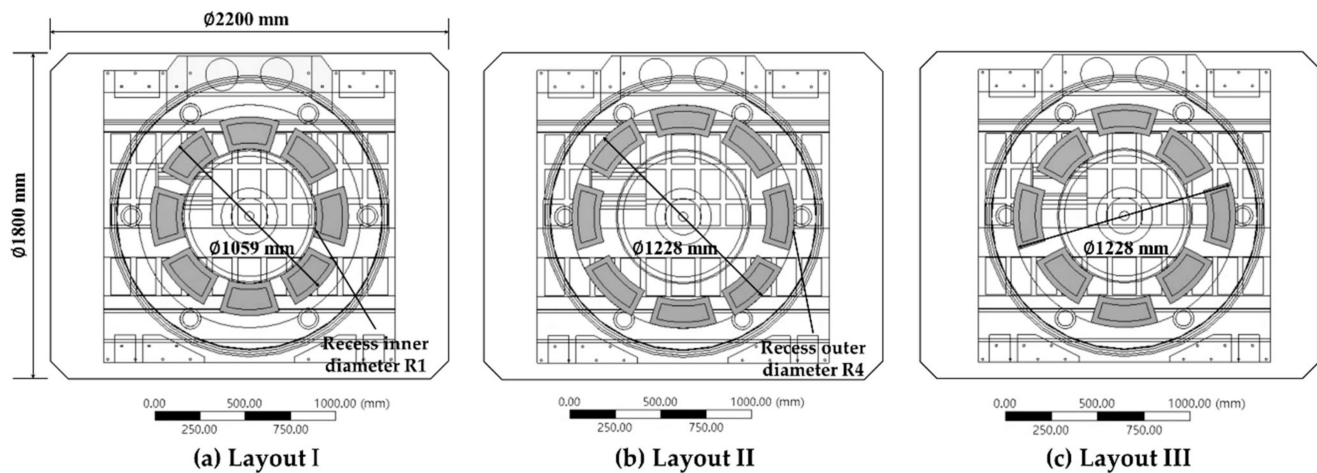**Figure 5.** Hydrostatic thrust bearing of rotary table (original layout).

(a)

(b)

Figure 6. Recess dimensions of new hydrostatic thrust bearing. (**a**) Recess of maximum diameter; (**b**) recess of minimum diameter.

Table 2. New recess dimensions.

Dimension	Recess of Maximum Diameter	Recess of Minimum Diameter
θ (deg)	35	35
R1 (mm)	459.5	371
R2 (mm)	492.5	404
R3 (mm)	581	515.85
R4 (mm)	614	548.85
Effective area (m^2)	0.03619	0.03619
Recess depth (mm)	2	2

Figure 7. Three layouts of hydrostatic thrust bearing.

2.1.2. Recess Flow Field Model

The recess flow field models were constructed according to the specifications in Tables 1 and 2 are shown in Figure 8a–d. Each of the four recess flow field models had an initial oil film thickness of 50 μm.
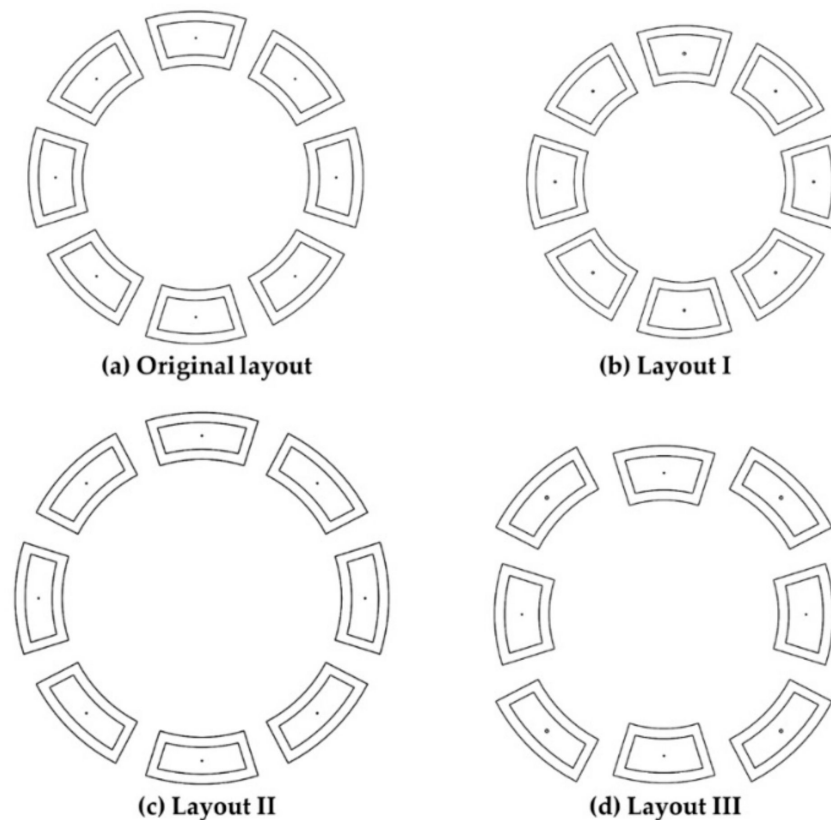
Figure 8. Flow-field model of different hydrostatic thrust bearing layouts.

2.1.3. Verification of Flow Field Model

While using ANSYS Fluent to model the flow field of hydrostatic thrust bearing, one important parameter in analysis is the length of capillary restrictor in designed film gap. In this study, we construct the hydrostatic bearing model in FLUENT, including the capillary restrictor. The length of capillary restrictor is calculated by using theoretical formula (shown in Equation (1)) and is then simulated by using FLUENT. Equation (1) is

the formula to calculate the length of capillary restrictor. *PS* is the supply pressure (20 bar) of the lubricant, P_r is the recess pressure of 10 bar. l_c is the length of capillary in mm, d_c is the inner diameter of the capillary (2 mm), μ_t is the viscosity of the lubricant in 0.0279 Pa.s (ISO VG32 oil). Q_{h0} is the outlet flow rate of the bearing recess at designed film gap.

$$l_c = \frac{\pi d_c^4 \times (P_s - P_r)}{128\mu_t Q_{h0}} \tag{1}$$

$$W = A_e \times P_r = \frac{P_s A_e}{1 + \frac{R_{c0}}{R_{h0}}(1 - \varepsilon)^3 \times \frac{R_c}{R_{c0}}} \tag{2}$$

Equation (2) calculates the load-carrying capacity (*W*) of the hydrostatic bearing. A_e is the effective area of the recess. R_{c0} is the flow resistance of capillary restrictor at designed film gap. R_c is flow resistance of capillary restrictor in final film gap. R_{h0} is the flow resistance of bearing sill at designed film gap. ε is the film gap displacement rate (or eccentricity rate) $\varepsilon = e/h_0$. e is the reduced film gap during loading condition. h_0 is the designed film gap. Since capillary restrictor is a fixed restrictor, the flow resistance of capillary restrictor is constant regardless the film gap. Therefore R_c/R_{c0} is one in any case. Figure 9 is the schematic diagram of capillary restrictor.
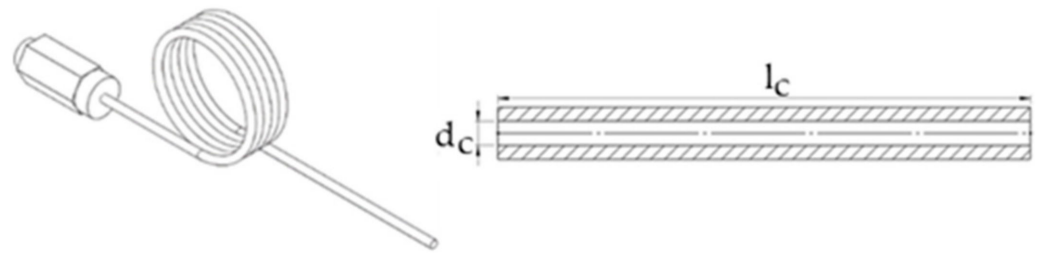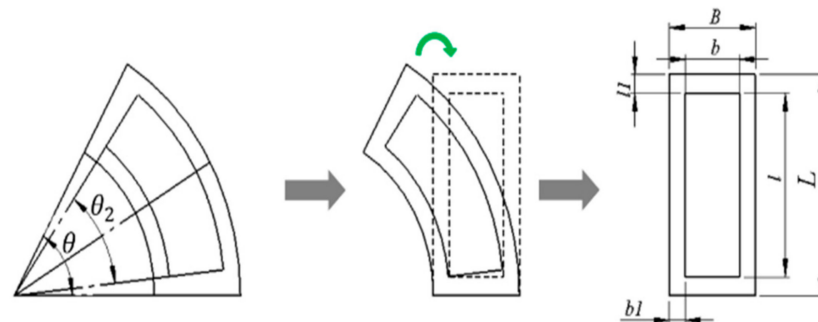

Figure 9. Schematic diagram of capillary restrictor.

The planar fan-shaped recess of hydrostatic thrust bearing design in this study is shown in Figure 10. Its effective area is calculated by Equation (3). The equivalent length of L and *l* is calculated by Equations (4) and (5), respectively.

$$A_e \approx \frac{1}{4}(L+l)(B + b) \tag{3}$$

$$L = \left(\frac{R_4 + R_1}{2}\right)2\pi\left(\frac{\theta}{360}\right) \tag{4}$$

$$l = \left(\frac{R_3 + R_2}{2}\right)2\pi\left(\frac{\theta_2}{360}\right) \tag{5}$$

Figure 10. Schematic diagram of equivalent conversion of flat fan-shaped recess.

Figure 11 depicts the outlet flow rate at four sills of the rectangular hydrostatic bearing pad. The equation to describe the oil flow of hydrostatic bearing pad is continuity equation.

That is to say, the inlet flow rate of the capillary must be equal to the sum of outlet rate through four bearing pad sills.
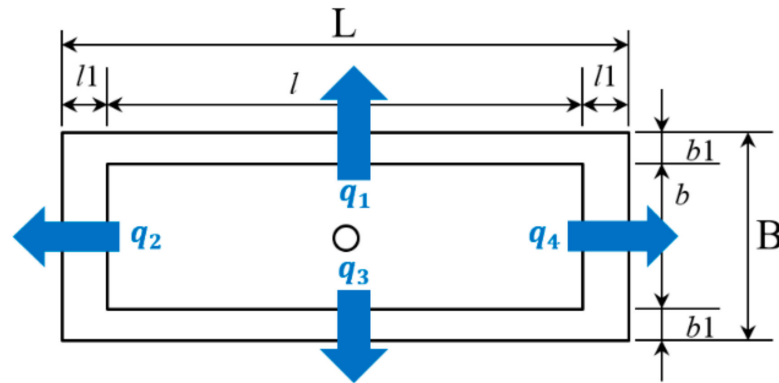
Figure 11. Outlet flow rate at four sills of the rectangular hydrostatic bearing pad.

For continuity equation of flow rate [31]: $Q_{inlet} = Q_{outlet}$

$$Q = Q_{h0} = Q_{c0} = \frac{\pi d_c^4 \times (P_s - P_r)}{128 \mu_t l_c} \tag{6}$$

Where Q_{c0} is the inlet flowrate of the capillary restrictor, Q_{h0} is the outlet flow rate of the four sills of the bearing pad. To calculate the flow rate for each sill:

$$q_1 = \frac{h_0^3 \times p_{r0} \times \left(L - \left(\frac{l_1}{2} \right) - \left(\frac{l_1}{2} \right) \right)}{12 \times \mu_t \times b_1} \tag{7}$$

$$q_2 = \frac{h_0^3 \times p_{r0} \times \left(B - \left(\frac{b_1}{2} \right) - \left(\frac{b_1}{2} \right) \right)}{12 \times \mu_t \times l_1} \tag{8}$$

$$q_3 = \frac{h_0^3 \times p_{r0} \times \left(L - \left(\frac{l_1}{2} \right) - \left(\frac{l_1}{2} \right) \right)}{12 \times \mu_t \times b_1} \tag{9}$$

$$q_4 = \frac{h_0^3 \times p_{r0} \times \left(B - \left(\frac{b_1}{2} \right) - \left(\frac{b_1}{2} \right) \right)}{12 \times \mu_t \times l_1} \tag{10}$$

Total outlet flow rate Q_{h0}:

$$Q_{h0} = q_1 + q_2 + q_3 + q_4 \tag{11}$$

From the flow continuity equation, the recess pressure and the load carrying capacity of the bearing pad can be calculated. The flow rate of all the hydrostatic thrust bearings in this research model were checked for their correctness by using continuity equation of oil flow.

2.2. Boundary Conditions of Stimulation

Following the construction of the flow field model, the data were imported into ANSYS software for pretreatment. The boundary conditions applied to the simulation of one-way fluid–structure interactions are as follows:

1. In the steady-state thermal and the static-structural models, the air-side natural convection temperature of the hydrostatic rotary table model was specified at 27 °C. Since this study only took into account the effects of oil film temperature rise on the hydrostatic rotary table, the simulated temperature rise distribution results of

the original and the three new hydrostatic axial thrust bearing designs (as obtained through ANSYS FLUENT software) were jointly incorporated into a structural heat-transfer model in order to perform one-way fluid-solid interactions. The simulated oil film temperature rise distribution results at a maximum rotational speed of 15 rpm were applied to the hydrostatic axial thrust bearing and the hydrostatic journal bearing, while the results at a maximum feed speed of 2 m/min were applied to all recesses in the closed-type hydrostatic slideway.

2. This study utilized the Joint_Type_Bushing structural model tool to simulate the oil film stiffness of all recesses at the initial oil film thickness. The initial oil film thickness of the recess served as the initial spacing between the structural models simulated through Joint_Type_Bushing. As shown in Figure 12a, the model spacing between the connector and the hydrostatic axial thrust bearing recess was 50 μm; the model spacing between the hydrostatic journal bearing recess and the connector was 50 μm. As shown in Figure 12b, the model spacing between the main and vice recesses and the fixed guide rail was 50 μm; the model spacing between the side recess and the fixed guide rail was 50 μm.

3. The contact conditions of the gear connector and the small gears in the gearbox are shown in Figure 13. The frictional contact type was selected here. The contact between the clamp and the gear connector was frictional, as shown in Figure 14. The contact condition between the ball screw and the fixed guide rail was bonded, as shown in Figure 15.

4. The maximum external load utilized in this study consisted of the maximum axial workpiece weight of 117,682 N and the maximum axial specific drilling force of 9348 N.
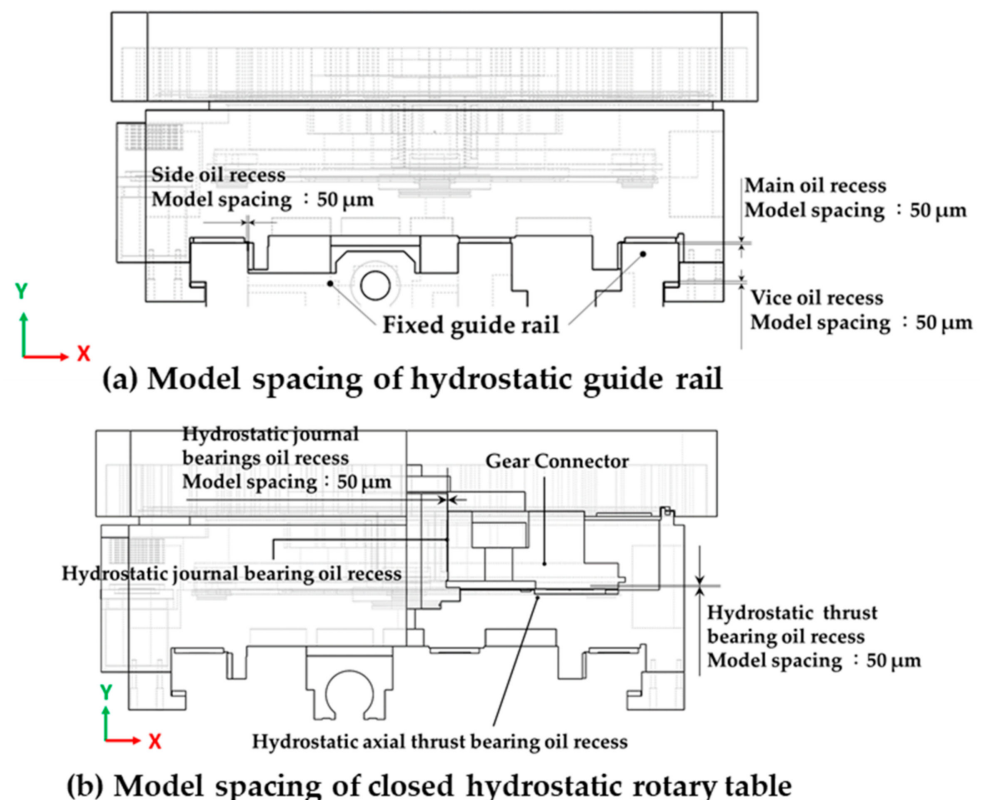

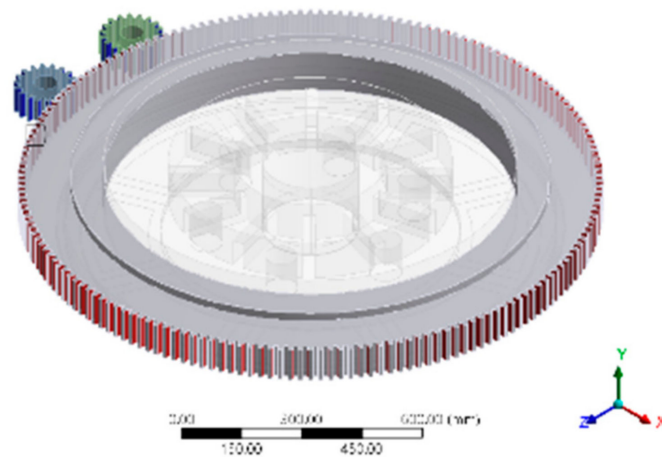Figure 12. Model spacing of structural analysis models.
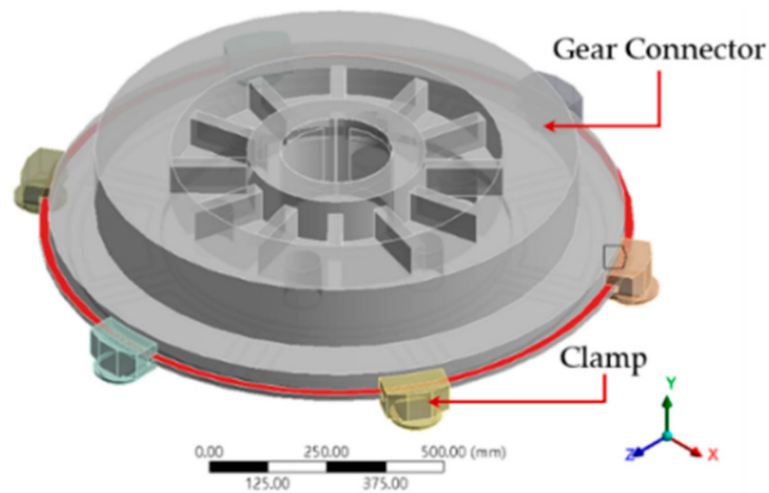
Figure 13. Gear contact conditions.

Figure 14. The contact condition between the clamp and the gear connector.
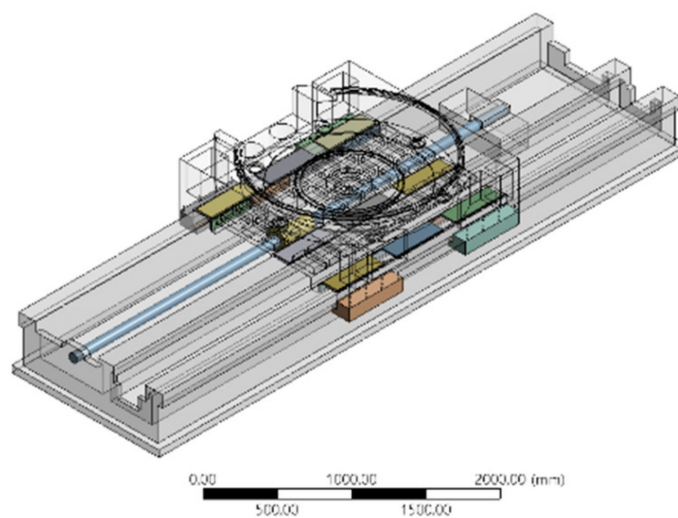

Figure 15. Contact condition of ball-screw and fixed guide rail.2.3. Methods of Simulation and Analysis.

First, FLUENT was used to simulate the oil-film temperature rise distribution of the original as well as the three different recess layouts of the hydrostatic axial thrust bearing. The simulation results were then imported into the steady-state thermal heat transfer model

to simulate the thermal deformation of the worktable. After the simulation was complete, the thermal deformation results were imported into the static-structural model to simulate the structural deformation of the worktable under an evenly distributed load as well as an eccentric load. Finally, the simulation results were compared in order to determine the layout with the smallest total deformation, that is, the optimal recess layout of the hydrostatic thrust bearing in a large-sized eccentric load-resistant hydrostatic rotary table for horizontal boring machine applications.

3. Analysis Results

3.1. Simulation Results of the Oil Film Temperature Field of Different Hydrostatic Thrust Bearing Layouts

Table 3 compares the outlet flow rates between the original, maximum-diameter, and minimum-diameter recesses. The maximum-diameter recess had the largest outlet flow rate, followed by the minimum-diameter recess, and then by the original recess. Based on these findings, even though the two new designs had larger outlet flow rates than the original, the increases in flow rates were rather marginal.

Table 3. Comparison of outlet flow rate between new recess and original recess.

	Outlet Flow Rate
Min. diameter recess	1.290×10^{-5} m^3/s
Max. diameter recess	1.460×10^{-5} m^3/s
Original recess	1.106×10^{-5} m^3/s

Table 4 shows the simulated maximum oil film temperatures of the original, maximum-diameter, and minimum-diameter recesses at a maximum rotating speed of 15 rpm. The maximum-diameter recess had the highest temperature, followed by the original recess, and then the minimum-diameter recess. Figure 16 depicts the oil film temperature rise distribution of the original and the three new hydrostatic thrust bearing recess layouts. When the rotational speed of the connector was fixed, the hydrostatic thrust bearing recesses had different tangential speeds at different layouts. The faster the tangential speed of a recess located farther away from the center of the rotary table, the higher its oil film temperature.

Table 4. Maximum oil film temperature of three recesses at 15 rpm.

	Max Oil Film Temperature
Min diameter recess	29.97 °C
Max diameter recess	30.58 °C
Original oil recess	30.02 °C
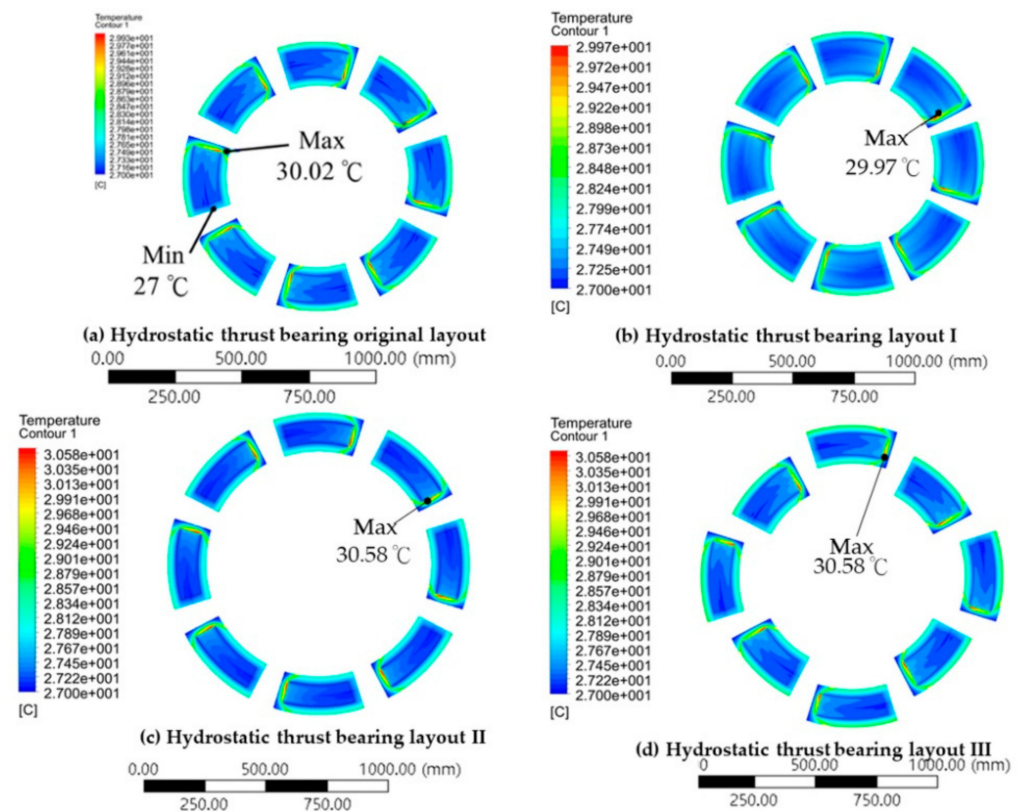
Figure 16. Oil film temperature rise of three layouts at 15 rpm.

3.2. Simulation Results of the Thermal Deformation of Worktable from Different Hydrostatic Thrust Bearing Layouts

The simulated oil film temperature distributions of the original and the three different recess layouts of the hydrostatic thrust bearing are shown in Figure 16. These results were imported into the static-structural and the steady-state thermal models to simulate the thermal deformation of the worktable structure, which is presented in Figure 17. Figure 17a depicts the simulation results of the thermal deformation of the table structure caused by the original recess layout of the hydrostatic axial thrust bearing. The maximum thermal deformation of the worktable was 11 μm. Figure 17b–d depict the simulation results of the thermal deformation of the worktable structure caused by the three different recess layouts of the hydrostatic thrust bearing. The maximum thermal deformations of the worktable at Layouts I, II, and III were 8.5 μm, 12 μm, and 11 μm, respectively. In short, Layout II caused the greatest thermal deformation on the worktable structure, followed by Layout III, the original layout, and then Layout I.
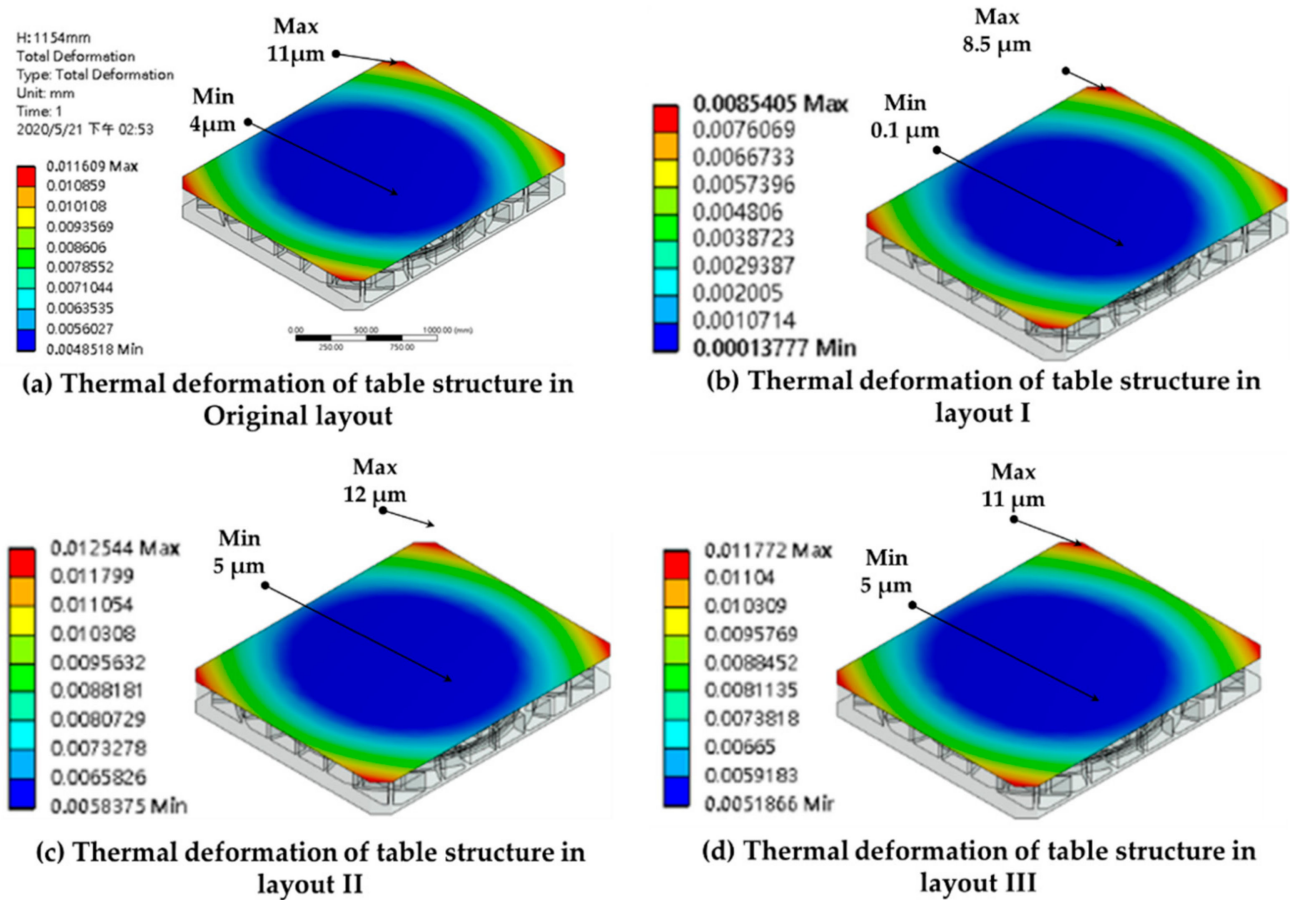
(a) Thermal deformation of table structure in Original layout

(b) Thermal deformation of table structure in layout I

(c) Thermal deformation of table structure in layout II

(d) Thermal deformation of table structure in layout III

Figure 17. Thermal deformation of worktable with different layouts.

3.3. Simulation Results of the Structural Deformation of the Worktable Caused by an Evenly Distributed Load

An evenly distributed load of 127,030 N, including the maximum axial workpiece weight of 117,682 N and the maximum axial specific drilling force of 9348 N, was applied onto the worktable, so as to simulate the structural deformations. A schematic of this procedure is shown in Figure 18.
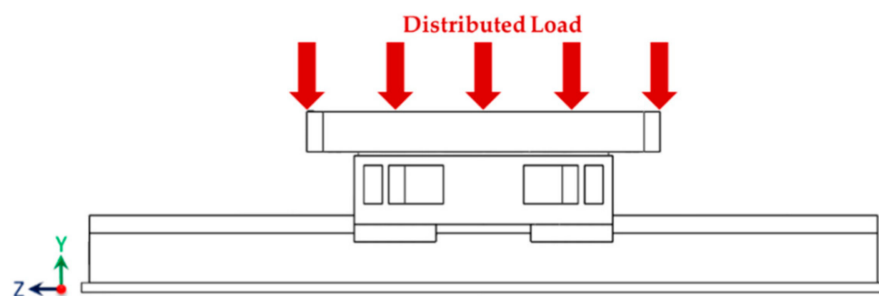

Figure 18. Schematic diagram of evenly distributed load on the worktable.

Figure 19 shows the simulation results of the structural deformation of the original and the three different recess layouts of the hydrostatic axial thrust bearing. Layout I caused the greatest worktable deformation, followed by Layouts II and III, which had similar results. Comparing between the deformation results, under an evenly distributed load, Layouts II and III had similar results and caused the smallest worktable deformation, while Layout I caused the greatest worktable deformation.
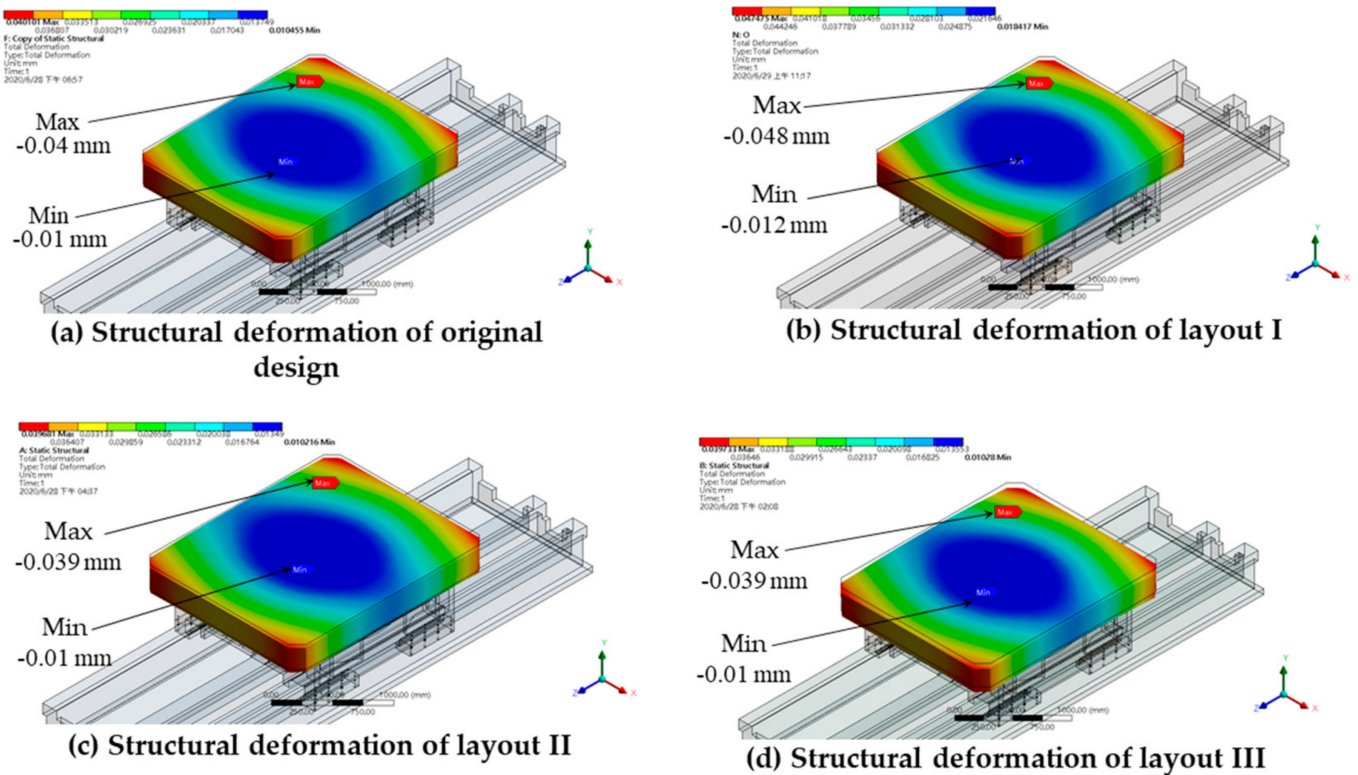
Figure 19. Structural deformation of the worktable with different hydrostatic thrust bearing layouts.

Comparing between the worktable deformation results caused by the original and the three different recess layouts of the hydrostatic axial thrust bearing, Layout I caused the largest deformation, followed by the original layout, and then by Layouts II and III. Layouts II and III caused similar deformations on the worktable, which was primarily due to them having the same (and maximum) recess layout diameter. Among the three different layouts, Layout I caused the largest deformation on the worktable, because the minimum recess layout diameter was used in this layout. The recess layout diameter used in the original layout was larger than that of Layout I; hence, the original layout caused a smaller deformation on the worktable compared to Layout I.

3.4. Simulation Results of the Structural Deformation of the Worktable Caused by an Eccentric Load

In reality, the center of mass of a workpiece is not always placed in the center of the worktable, and this lack of equilibrium can cause the worktable to tilt. This affects the machining accuracy of workpiece if the worktable deformation caused by an eccentric load is too large. In order to examine the maximum deformation caused by an eccentric load acting on the rotary worktable in this study, four zones (A, B, C, and D) were drawn out, such that the eccentric load applied on each zone had the longest diagonal, as shown in Figure 20.
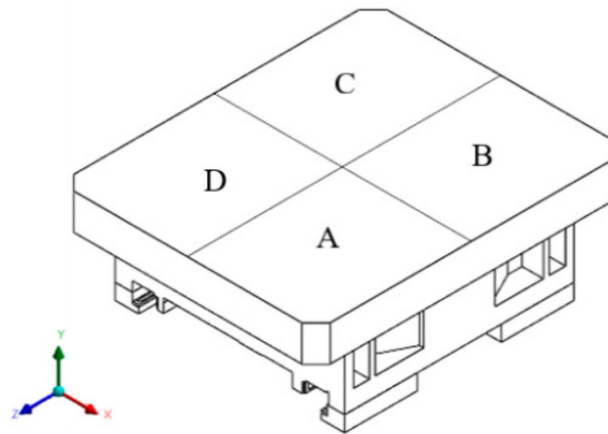
Figure 20. Four zones (A to D) to apply maximum eccentric load on worktable.

Figure 21a–b show the simulation results of the worktable deformation when the maximum eccentric load was applied on Zones A and B. The structural deformation in Zones A and B ranged from 0.0015 mm to −0.142 mm and 0.0019 mm to −0.142 mm, respectively. Figure 21c,d show the simulation results of the worktable deformation when the maximum eccentric load was applied on Zones C and D. The structural deformation in Zones C and D ranged from 0.0015 mm to −0.145 mm and 0.0014 mm to −0.143 mm, respectively.
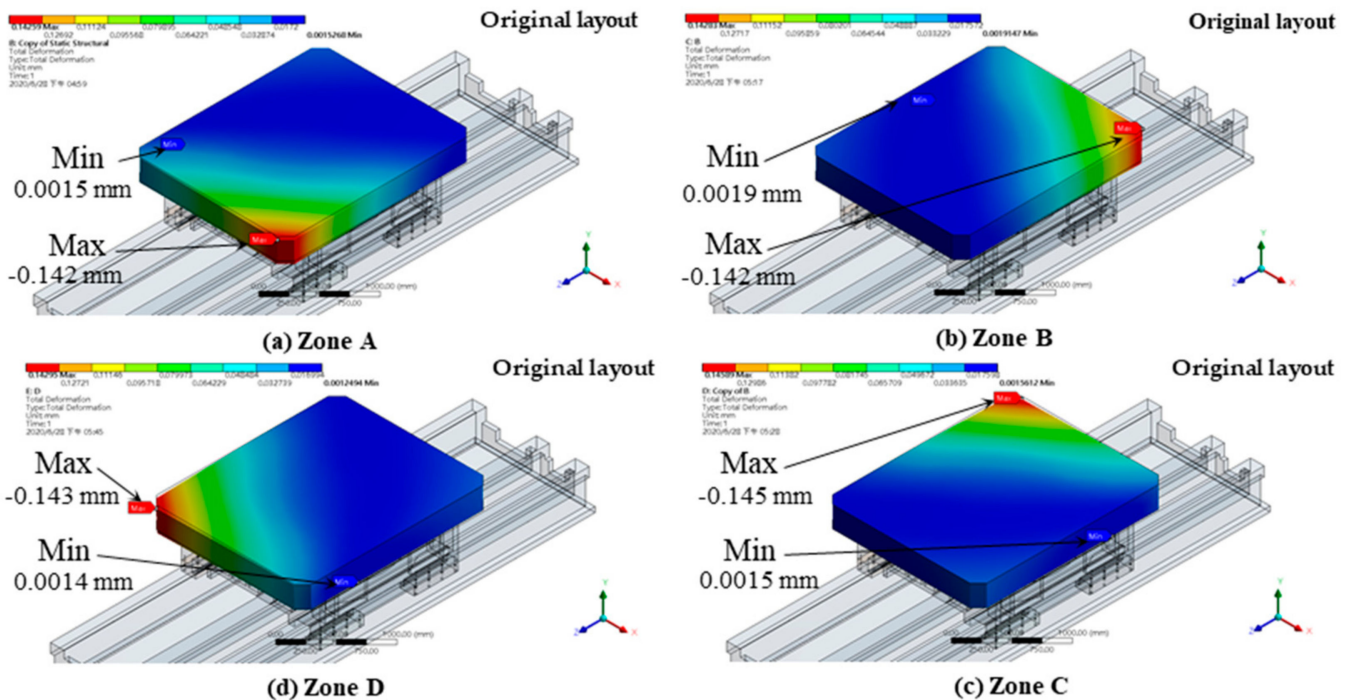

Figure 21. Structural deformation of the worktable: original layout under maximum eccentric load.

Figures 21–24 show the simulation results of the worktable deformation when the maximum eccentric load was applied to each of the four zones in the three different recess layouts of the hydrostatic thrust bearing. Table 5 lists the simulation results of the worktable deformation magnitude when the maximum eccentric load was applied in the three different recess layouts of the hydrostatic axial thrust bearing. According to Table 5, the greatest worktable deformation occurred when the maximum eccentric load was applied to Zone C in all three layouts.
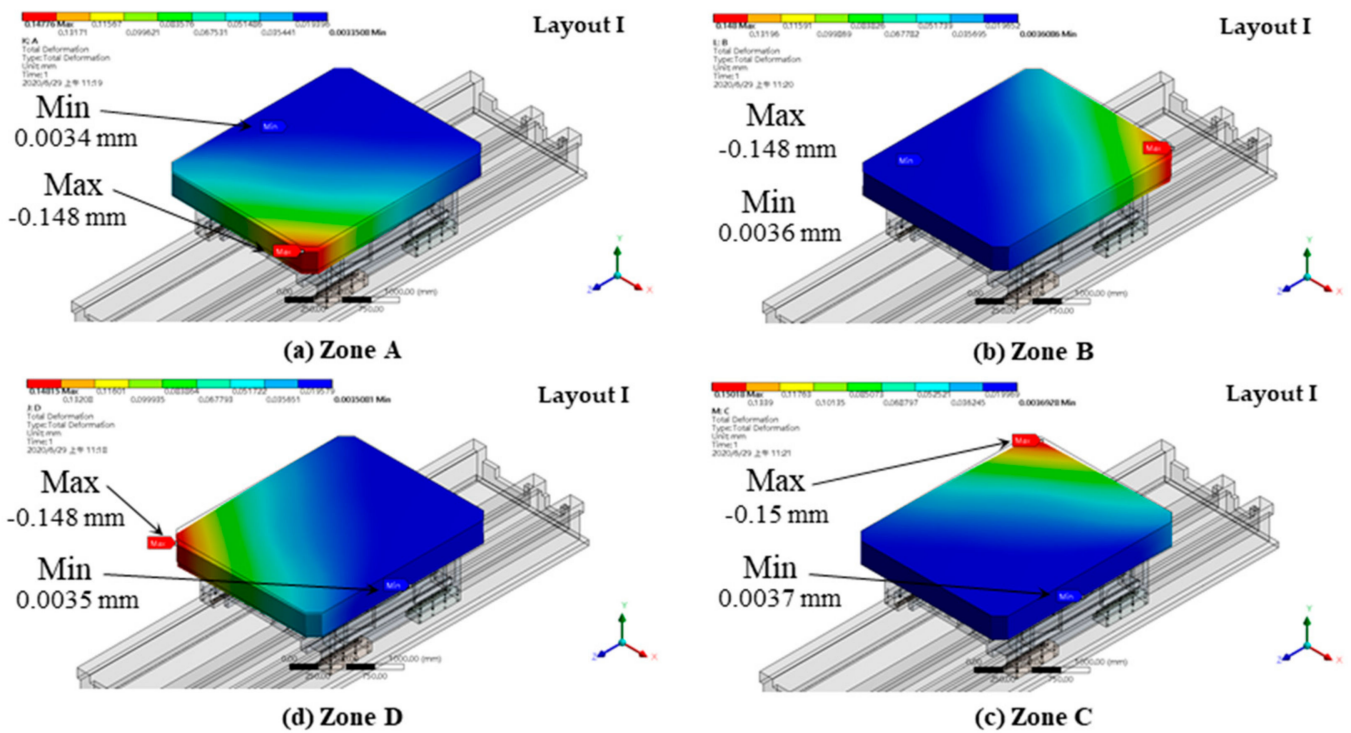
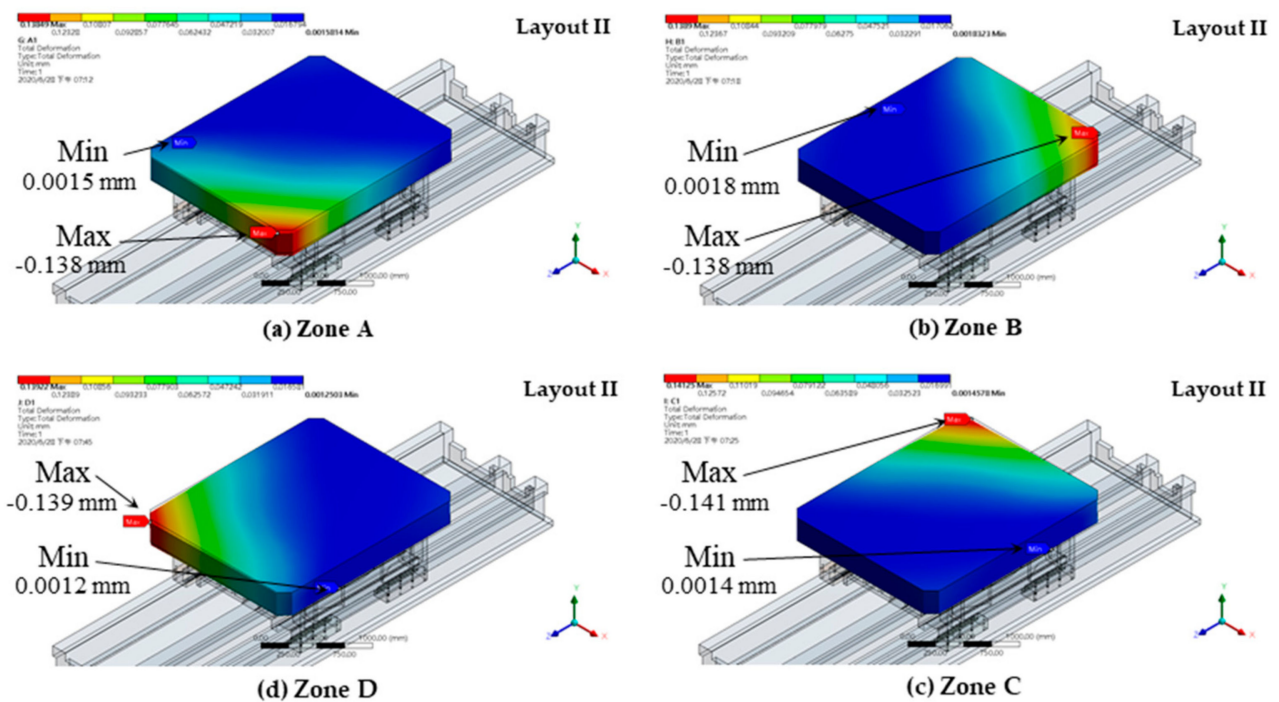**Figure 22.** Structural deformation of the worktable: Layout I under maximum eccentric load.

Figure 23. Structural deformation of the worktable: Layout II under maximum eccentric load.
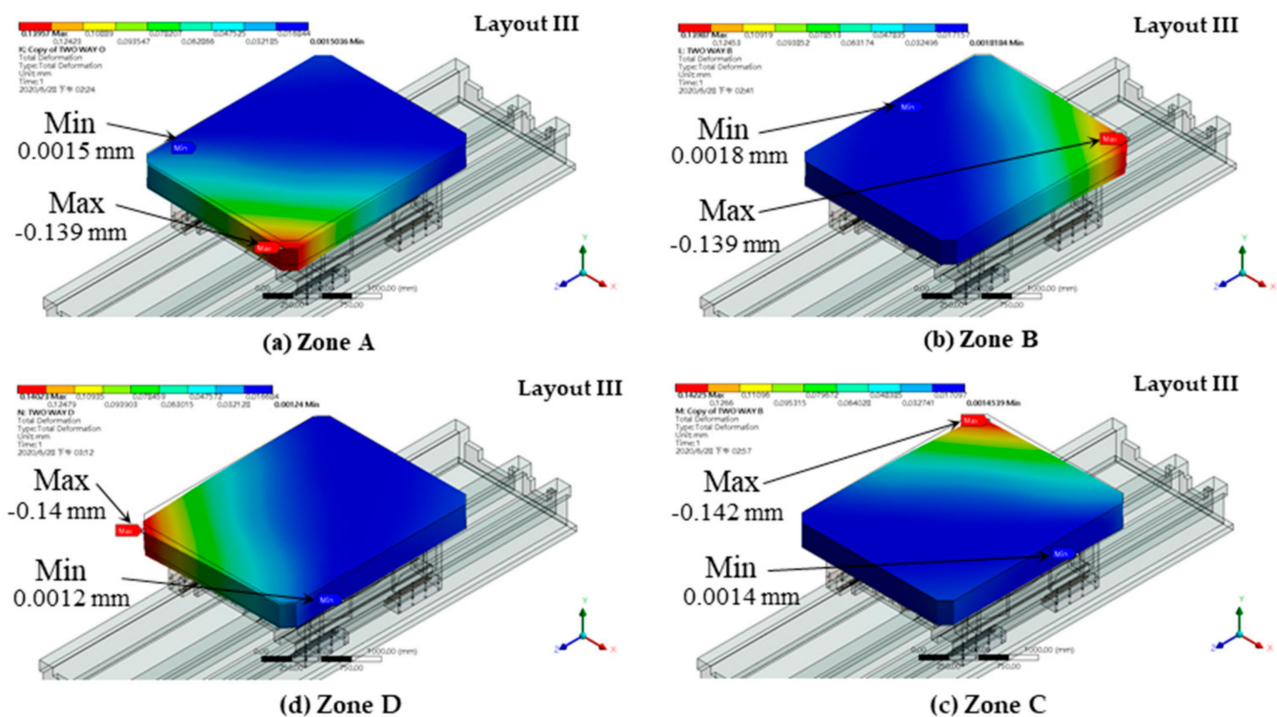
Figure 24. Structural deformation of the worktable: Layout III under maximum eccentric load.

Table 5. Comparison of worktable deformation magnitude under eccentric load in various zones and layouts.

Eccen. Load / Layout	Layout I Deformation (mm)		Layout II Deformation (mm)		Layout III Deformation (mm)	
Zone	Min	Max	Min	Max	Min	Max
A	0.0034	−0.148	0.0015	−0.138	0.0015	−0.139
B	0.0036	−0.148	0.0018	−0.138	0.0018	−0.139
C	0.0037	−0.150	0.0014	−0.142	0.0014	−0.141
D	0.0035	−0.148	0.0012	−0.139	0.0012	−0.140

Regardless of the original or of the three different recess layouts of the hydrostatic thrust bearing, the largest worktable deformation occurred when the maximum eccentric load was applied to Zone C. This was primarily due to the structural effects of the closed-type hydrostatic slideway. Figure 25 shows the bottom view of the hydrostatic worktable, in which the circled area highlights the long rear span of the guide rail, which weakened its support strength. Therefore, this study used the maximum deformation at Zone C as a reference to compare between the maximum worktable deformation under the original and the three different recess layouts. As shown in Table 6, the largest deformation occurred in Layout I, followed by the original layout, Layout II, and then by Layout III. Based on the simulation results, the maximum worktable deformations in Layouts II and III were marginally close, which was mainly due to the same hydrostatic bearing diameter of 1228 mm. Since Layout III was a dual-ring layout, the worktable deformation was smaller. Layout I had the largest deformation, as the smallest hydrostatic bearing diameter (1059 mm) was used.
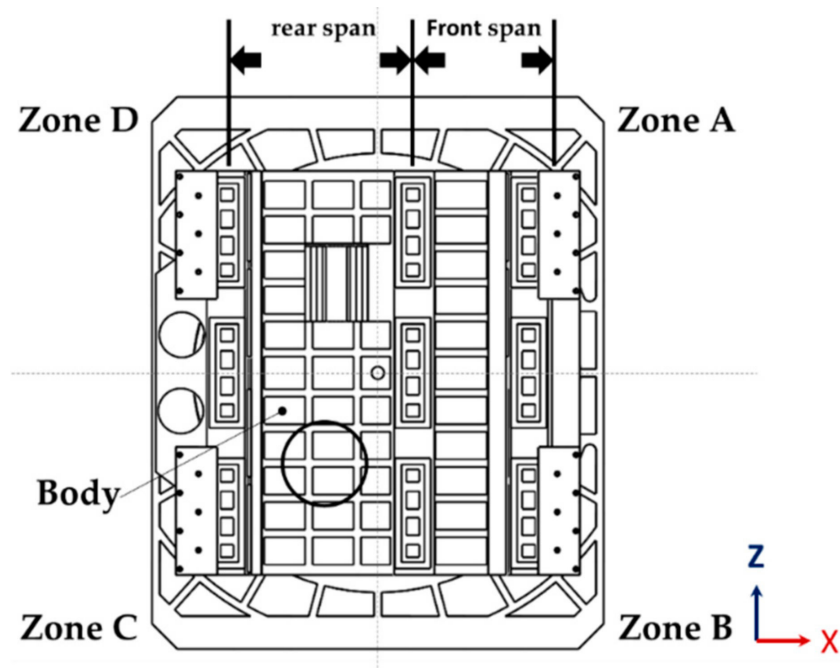
Figure 25. Bottom view of the hydrostatic worktable.

Table 6. Simulation results of the eccentric load deformation of the three hydrostatic axial thrust bearings.

	Maximum Deformation
Layout I	−0.150 mm
Layout II	−0.142 mm
Layout III	−0.141 mm
Original layout	−0.145 mm

4. Analysis Results and Discussion

The simulation and analysis results and discussion for this section are as follows:

1.　Under the evenly distributed load and eccentric load conditions, Layout III had the smallest worktable deformation among the four layouts, while Layout I had the largest deformation under both conditions. These results show that the larger the recess layout diameter, the greater the recess's resistance against the tilting moment, which reduced the structural deformation of the worktable.
2.　The thermal deformation caused by Layout II was the largest among the four layouts, while Layout I had the smallest thermal deformation.
3.　When the rotational speed of the rotary table was fixed, a hydrostatic thrust bearing recess placed farther away from the center of the worktable would experience a faster tangential speed, which increased the oil film temperature.

5. Conclusions

This study sought to explore the resistance of the recess of a hydrostatic thrust bearing against the tilting moment in the largest diametric space from within the gear connector of a rotary table (i.e., the table's resistance against an eccentric load). Three layouts of the recess of the hydrostatic thrust bearing were designed (two single-ring layouts that involved the maximum and minimum diameter, respectively, as well as a dual-ring layout). One-way fluid–solid interactions were modeled through ANSYS software to simulate and analyze the thermal deformation and the eccentric load deformation of the rotary table structure in the three different recess layouts of the hydrostatic thrust bearing. The advantages

and drawbacks of all three layouts in terms of the worktable's structural and thermal deformations were then compared. Finally, this study proposes several recommendations for the recess layout designs of a hydrostatic thrust bearing. The conclusions are as follows:

1. The layout diameter of the hydrostatic thrust bearing recess has a significant effect on the worktable's resistance against an eccentric load. A dual-ring recess layout offers better resistance against the tilting moment compared to a single-ring layout while, in single-ring layouts, a larger layout diameter offers better resistance against the tilting moment compared to a smaller layout diameter.

2. If one chooses a recess layout based on the rotary table's resistance against the tilting moment, the oil film temperature must also be taken into account, due to the reduced recess dimensions in a limited structural space. Moreover, the recess of a hydrostatic thrust bearing placed further away from the center of the worktable experiences a faster tangential speed, which increases the oil film temperature. In Layout II, eight recesses were placed within the range of the maximum layout diameter, which resulted in the largest thermal deformation of the worktable; in Layout III, only four recesses were placed within that range, which caused a medium thermal deformation; in Layout I, the minimum layout diameter was used, which resulted in the smallest thermal deformation.

A recommendation for future work is the analysis of the total deformation effect of the eccentric load acting on the linear slideway base structure beneath the hydrostatic rotary table by considering three different layouts. This may improve understanding of the overall deformation of the hydrostatic slideway rotary table in horizontal boring machine applications.

Nomenclature

A_e	effective area of recess	P_s	supply pressure
B	width of bearing pad	P_r	recess pressure
b	width of recess	Q_{c0}	flow rate of capillary at designed film gap
b_1	sill of bearing pad in width direction	Q_{h0}	outlet flow rate of bearing sills designed film gap
d_c	inner diameter of capillary	Q_{outlet}	outlet flow rate of the recess
e	eccentricity	Q_{inlet}	inlet flow rate of the recess
ε	eccentricity rate	$q_{1,2,3,4}$	flow rate at sill 1, 2, 3, 4
h_0	designed film gap	R_1	inner radius of the bearing pad
L	length of bearing pad	R_2	inner radius of the recess
l	length of recess	R_3	outer radius of the recess
l_1	sill of bearing pad in length direction	R_4	outer radius of the bearing pad
l_c	length of capillary	R_c	flow resistance of the capillary

θ	angle of the recess	R_{c0}	flow resistance of the capillary at designed film gap
μ_t	viscosity of the lubricant oil	R_{ho}	flow resistance of the bearing sills at designed film gap
W	Load-carrying capacity of the bearing pad		

References

1. Slocum, A.H. *Precision Machine Design*; Society of Manufacturing Engineers: Tripadvisor, MI, USA, 1992.
2. Rowe, W.B. *Hydrostatic and Hybrid Bearing Design*; Butterworth: Oxford, UK, 1983.
3. Bassani, R.; Piccigallo, B. *Hydrostatic Lubrication*; Elsevier: Amsterdam, The Netherlands, 1992.
4. Harnoy, A. *Bearing Design in Machinery: Engineering Tribology and Lubrication*; CRC Press: Boca Raton, FL, USA, 2002.
5. Rowe, W.B. *Hydrostatic, Aerostatic and Hybrid Bearing Design*; Butterworth-Heinemann: Oxford, UK, 2012.
6. Lee, H.B.; Oh, J.H.; Oh, C.H.; Choi, Y.H. Structural Design Optimization of the Rotary Table of a Floor Type Boring Machine for Minimum Weight and Compliance by using GA. *Appl. Mech. Mater.* **2013**, *271–272*, 1421–1426. [CrossRef]
7. Shie, J.S.; Shih, M.C. A Study on Optimum Design and Dynamic Behavior of a Hydrostatic Guideway on Rotary Machine Tool. In Proceedings of the 2013 CACS International Automatic Control Conference, Sun Moon Lake, Taiwan, 2–4 December 2013.
8. Wang, S.; Du, X.; Li, M.; Cao, Z.; Wang, J. Analysis of Temperature effect on the Lubricating State of Hydrostatic Bearing. *J. Theory Appl. Inf. Technol.* **2013**, *48*, 817–821.
9. Srinivasan, V. Analysis of Static and Dynamic Load on Hydrostatic Bearing with Variable Viscosity and Pressure. *Int. J. Sci. Technol.* **2013**, *6*, 4777–4782. [CrossRef]
10. Zhao, J.; Liang, Y.; Gao, D. Oil Pocket's Bearing Capacity Analysis of Liquid Hydrostatic Worktable in Gantry Moving Milling Center. *Chin. J. Mech. Eng.* **2014**, *27*, 1008–1017.
11. Zhang, H. Research on the Application of Constant Pressure Closed Static Pressure Guideway for the Guideway of Heavy CNC Floor Milling and Boring Machine. *Mech. Eng.* **2016**, *6*, 133–134. (In Chinese) [CrossRef]
12. Zhang, Y.; Liu, G.; Yang, X.; Hu, C.; Wang, H.; Shao, J. Coupled Solving Thermal Deformation of Hydrostatic Bearing Rotary Worktable Based on Temperature Fields of Oil Film. *J. Comput. Theory Nanosc.* **2015**, *12*, 3917–3921. [CrossRef]
13. Wang, Y.; Zhao, Y.; Cai, L.; Liu, Z.; Cheng, Q. Effects of Thermal and Hydrodynamic Characteristics of Heavy-Duty Rotary Table on the Hydrostatic Circular Pads. *J. Vibroeng.* **2016**, *18*, 4193–4206.
14. Wang, J.; Yin, Y.; Liu, Z. Study on Dynamic Characteristics of Oil Film of Hydrostatic Rotary Table Considering the Effect of Unbalance Load and Roughness. In Proceedings of the 2016 International Conference on Applied Mechanics, Mechanical and Materials Engineering (AMMME 2016), Xiamen, China, 18–19 December 2016.
15. Wang, Y.; Liu, Z.; Cai, L.; Cheng, Q.; Dong, X. Optimization of Oil Pads on a Hydrostatic Turntable for Supporting Energy Conservation Based on Particle Swarm Optimization. *J. Mech. Eng.* **2018**, *64*, 95–104.
16. Chang, J.H. The Study on Hydrostatic Bearing Design for the Table of Horizontal Boring Machine. Master's Thesis, National Kaohsiung University of Science and Technology, Kaohsiung, Taiwan, 2018.
17. Kettleborough, C.F. The Stepped Thrust Bearing—A Solution by Relaxation Methods. *J. Appl. Mech.* **1954**, *21*, 19–24. [CrossRef]
18. Johnston, R.C.R.; Kettleborough, C.F. An Experimental Investigation into Stepped Thrust-Bearings. *Proc. Inst. Mech. Eng.* **1956**, *170*, 53–54. [CrossRef]
19. Kettleborough, C.F. The Hydrodynamic Pocket Thrust-Bearing. *Proc. Inst. Mech. Eng.* **1956**, *170*, 55–56. [CrossRef]
20. Kettleborough, C.F. The Tapered-Land Thrust Bearing. *J. Appl. Mech.* **1956**, *23*, 581–583. [CrossRef]
21. Kettleborough, C.F. An Approximate Analytical Solution for the Stepped Bearing. *J. Appl. Mech.* **1961**, *28*, 507–510. [CrossRef]
22. Hahn, E.J.; Kettleborough, C.F. Solution for the Pressure and Temperature in an Infinite Slider Bearing of Arbitrary Profile. *J. Lubr. Technol.* **1967**, *89*, 445–452. [CrossRef]
23. Hahn, E.J.; Kettleborough, C.F. The effects of thermal expansion in infinitely wide slider bearings—Free thermal expansion. *J. Lubr. Technol.* **1968**, *90*, 233–239. [CrossRef]
24. Hahn, E.J.; Kettleborough, C.F. Thermal Effects in Slider Bearings. *Proc. Inst. Mech. Eng.* **1968**, *183*, 53–55. [CrossRef]
25. Kettleborough, C.F. Hydrodynamic Induced Vibrations in Accelerated Thrust Bearings. *J. Mech. Eng. Sci.* **1974**, *16*, 69–70. [CrossRef]
26. Gohar, R.; Rahnejat, H. *Fundamentals of Tribology*, 3rd ed.; World Scientific: Singapore, 2018.
27. Coombs, J.A.; Dowson, D. An Experimental Investigation of the Effects of Lubricant Inertia in a Hydrostatic Thrust Bearing. *Proc. Inst. Mech. Eng.* **1964**, *179*, 270–272. [CrossRef]
28. Safar, Z.S. Adiabatic solution of a tilted hydrostatic thrust bearing. *Wear* **1983**, *86*, 133–138. [CrossRef]
29. Yang, X.D.; Shao, J.P.; Xu, X.Q.; Wang, Y.F.; Yin, C.; Jiang, H. Research on Velocity Influence on Thermal Deformation Field of Heavy Hydrostatic Thrust Bearing. *Adv. Mater. Res.* **2010**, *129–131*, 968–972. [CrossRef]
30. Li, X.; Wang, X.; Li, M.; Ma, Y.; Huang, Y. The research status and progress of heavy/large hydrostatic thrust bearing. *Adv. Mech. Eng.* **2014**, *6*, 982584. [CrossRef]
31. Yang, S.-H. Design and Performance Evaluation of a Hydrostatic Rotary Table for Horizontal Boring Machines. Master's Thesis, National Kaohsiung University of Science and Technology, Kaohsiung, Taiwan, 2020.